



Special Issue at the occasion of the ISMA2018 International Noise and Vibration Conference

A method for the observation of the anelastic behaviour of anisotropic porous materials using digital image correlation



Luca Manzari^{a,*}, Huina Mao^a, Peter Göransson^a, Jacques Cuenca^b,
Inés López Arteaga^{a,c}

^a KTH Royal Institute of Technology, Aeronautical and Vehicle Engineering, Teknikringen 8, SE-10044, Stockholm, Sweden

^b Siemens Industry Software, Interleuvenlaan 68, B-3001, Leuven, Belgium

^c Eindhoven University of Technology, Department of Mechanical Engineering, 5600 MB, Eindhoven, the Netherlands

ARTICLE INFO

Article history:

Received 19 June 2019

Revised 23 December 2019

Accepted 10 February 2020

Available online 11 February 2020

Handling Editor: I. Trendafilova

Keywords:

Poroelastic media

Anisotropy

Anelasticity

Digital image correlation

Inverse estimation

ABSTRACT

This paper proposes an experimental method for observing the anelastic anisotropic behaviour of poroelastic media. The setup relies on three-dimensional digital image correlation, enabling the acquisition of full-field displacement data from the visible faces of a vibrating cubic material sample. The latter is placed in a vacuum chamber, loaded with a seismic mass and excited uniaxially. The observability and relevance of the three-dimensional displacement field is assessed by means of a numerical simulation. A homogenised fully anisotropic model is used, implemented using the finite element method. Thus, a set of material properties obtained using single-point data is considered as the reference configuration for the numerical method. Selected experimental and numerical results are presented, highlighting the importance and the advantages that full-field observations yield over single-point measurements.

© 2020 The Authors. Published by Elsevier Ltd. This is an open access article under the CC BY license (<http://creativecommons.org/licenses/by/4.0/>).

1. Introduction

A major challenge in modelling the dynamic behaviour of poroelastic media is the choice of a constitutive model relying on experimentally observable parameters. A significant number of models for porous media exist [1], where the choice for a particular framework is dictated by the type of porous material or the experimental conditions under consideration. In the present work, the focus is the experimental characterisation of the viscoelastic properties of the solid phase, or frame, of open-cell foams.

In the absence of a fluid, open-cell foams behave as viscoelastic solids [2–5], which arises as a special case in the Biot modelling framework [6–8]. Previous work by the team of the authors has dealt with investigating the characterisation of open-cell foams by placing these in a vacuum chamber [9,10,19]. An inverse method is used therein and provides a macroscopic estimation of the anisotropic Hooke matrix, anelastic relaxation properties and orientation of the natural material coordinates. The chosen experimental setup consisted of placing the sample between a shaker foundation and a seismic mass, the experimental data consisting of transfer functions obtained by laser Doppler vibrometry.

Laser vibrometry is common as a non-contact measurement method of relatively low complexity for accessing the dynamic viscoelastic behaviour of poroelastic media [11,12]. However, the characteristic strut thickness of an open cell foam is several

* Corresponding author.

E-mail address: manzari@kth.se (L. Manzari).

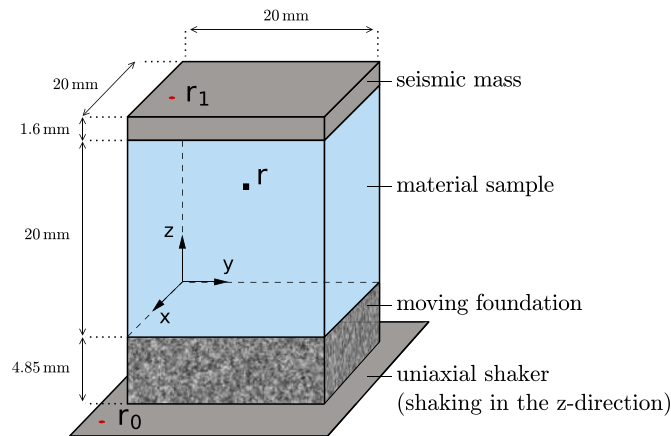


Fig. 1. Schematic representation of the proposed setup. The velocity at points \mathbf{r}_0 and \mathbf{r}_1 is scanned by the laser vibrometer as a stationarity check. The camera systems measures the three-dimensional displacement $\mathbf{u}(\mathbf{r}) = (u_x, u_y, u_z)$ at a set of points $\mathbf{r} = (x, y, z)$ on the front face. The (x, y, z) coordinate system is centred on one of the lower corners of the sample.

times smaller than the typical beam spot diameter of a laser Doppler vibrometer [13–15]. This results in the measured velocity being a local average within the volume of focus of the laser, whose depth increases with porosity, possibly contributing to uncertainties observed in previous inter-laboratory tests [11]. Furthermore, an underlying limitation of the above methods is the lack of observability of shear motion in the material under the chosen loading configurations, as pointed out for instance in Ref. [10].

In the present paper full-field displacement data is obtained by means of three-dimensional dynamic digital image correlation, using two high-speed cameras. A similar setup to that in Ref. [10] is used, including a vibrating base and a seismic mass. Observations of the dynamic deformation of a melamine foam are provided and then compared to numerical simulations based on previously obtained parameter values for the same material using a set of single-point measurements.

The central motivation for the experimental approach developed here is that a larger amount of data (i.e. the three-dimensional displacement field of the four exposed sides of the sample and the foundation) will enable an over-determination of the parameter search procedure, thus reducing its complexity and therefore potentially limiting the appearance of local minima. The numerical method used herein is capable of replicating the experiment, thus providing a framework for effectively increasing the number of equations to solve, while keeping the number of unknown parameters unaltered, thus rendering the model inversion procedure more robust.

The paper is organised as follows. The experimental setup is described in Section 2. The material model and its numerical implementation are presented in Section 3. Section 4 defines the transfer functions used for numerical design exploration and results are shown in Section 5.

2. Data acquisition

This section presents the general aspects of the experimental setup and data acquisition procedure proposed in the present work. The development of the test rig and its components is thoroughly described in Ref. [16], along with a flow-chart describing the measurement procedure. Guidelines for the use of a laser vibrometer for choosing suitable excitation levels are also provided therein, based on a real-time estimation of the dynamic strain experienced by the sample in the direction of the excitation. Note that in the present work the per-frequency, laser-aided autoranging has not been performed. For completeness, a brief description of the measurement procedure is given in schematic form in Algorithm 2.1. A detailed description of the derivation of transfer functions from the measured displacement fields is given in Ref. [17].

2.1. Experimental setup

A schematic representation of the proposed setup is given in Fig. 1.

The experimental setup consists of a vertical electrodynamic shaker on top of which a rigid foundation supports the material sample under consideration, depicted in Fig. 2 (a). A seismic mass of 1.73 g is placed on top of the sample in order to enforce resonant features in the motion within a low frequency range [12]. A pair of high-speed cameras placed outside the vacuum chamber records the sample and the foundation through a transparent poly(methyl methacrylate) window (see Fig. 2 (b)). The acquisition is performed sequentially on one face of the sample at a time. A rotation stage supporting the shaker assembly allows for a controlled rotation of the setup while avoiding to open the chamber, thus preserving stable vacuum conditions across acquisitions. The pressure in the vacuum chamber is automatically kept below a set threshold by a microcontroller. The latter is also responsible for turning on the lighting unit only for the camera acquisition time, so as to reduce thermal perturbations.

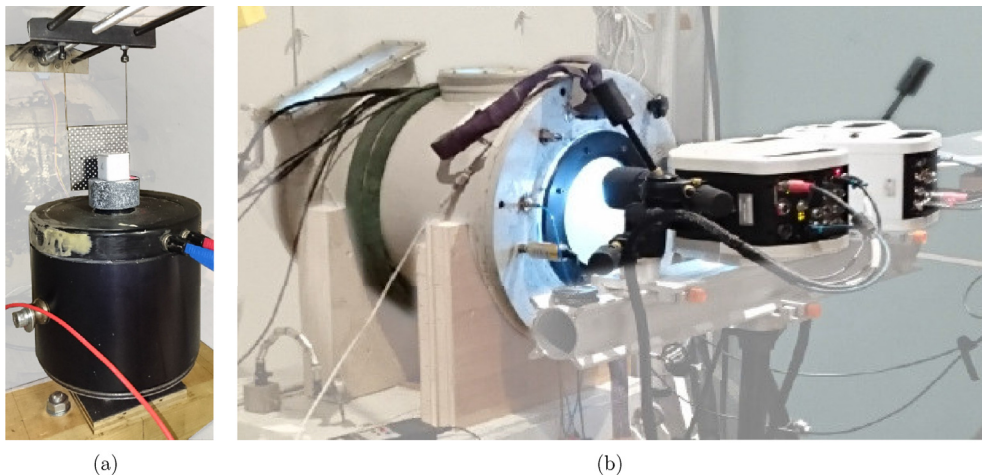


Fig. 2. Detailed and global views of the setup. (a) Inner view of the vacuum chamber with sample mounted on the shaker (in turn mounted on a motorised rotation base), calibration plate suspended from motorised translation rail. (b) Outer view of the setup during a measurement where the light, high-speed cameras and laser vibrometer are visible.

The shaker is excited with a monochromatic (i.e. single frequency, sinusoidal) signal. The frequencies of interest are visited in a random sequence in order to minimise the perturbation of a given observation with material relaxation processes at previously excited neighbouring frequencies. The data acquisition process is automatic, thus maximising the repeatability and reproducibility of the tests.

Algorithm 1 Brief description of the measurement procedure.

```

begin
  randomize list of frequencies of interest;
  place sample on shaker in vacuum chamber;
  close vacuum chamber;
  pull vacuum;
  for each face of the sample do
    rotate shaker such that the face being imaged is visible to both cameras;
    for each frequency in list of frequencies do
      turn on signal generator at frequency of interest;
      wait 2s for sample to reach steady state;
      turn on illumination unit;
      wait 2s for lighting conditions to be stable;
      send trigger to the cameras;
      acquire video and voltage sent to the shaker power amplifier;
      turn off illumination unit and signal generator;
      move video from camera RAM to permanent storage;
  
```

2.1.1. Equipment used, recording parameters, DIC parameters

For the results presented in this paper, two Phantom v1612 high-speed cameras equipped with AF Micro-Nikkor 200 mm f/4D IF-ED lenses stepped down to f/32 have been used, capturing 50 stereo frames per frequency with an exposure time of 240μ s at a rate of 4000 fps. A useable area of interest of $\approx 23.8 \times 29.7$ mm has been imaged with a 12 bit monochromatic sensor at a resolution of 640×800 px.

The calibration of the system has been performed using the proprietary software LaVision Davis 8.3, using an ad-hoc distortion model (described in Ref. [23]) implemented in Davis as a “3rd order polynomial model” [21]. The RMS of the reprojection error after calibration is 0.077px. The DIC has also been performed in Davis, using an iterative least-squares matching algorithm (see Ref. [22]) with a window size of 19×19 px and a 4px step size.

2.2. Data processing

Due to the specific configuration of the present setup, the displacement fields produced by digital image correlation are not useable in their raw form. Indeed, specular reflections on the foam struts may cause the algorithm to fail locally and therefore

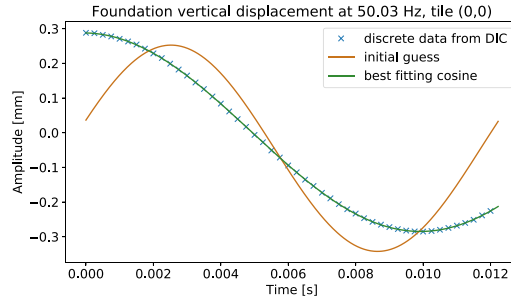


Fig. 3. Vertical displacement of a subset of the foundation, as computed by the DIC algorithm using 50 frames. An initial guess for a best fitting cosine is performed using a Fast Fourier Transform to estimate frequency and phase, the standard deviation as an estimator of the amplitude and the mean value as an estimator of the offset. Such guess is fed to a non-linear optimisation algorithm, and the best fitting cosine is found.

linear interpolation in time is used whenever such failures cause momentary loss of information. In addition, the coordinates at which the data is obtained are relative to the initial view of the calibration plate. Therefore, a transformation is applied in order for the reference coordinate system to be that of the rigid foundation at rest. This is performed for every frame by applying principal component analysis (PCA) to the height map of the foundation, assumed non-deformable [17].

The motion of the foam is quantified by exploiting the fact that the excitation is monochromatic. Indeed, a pure sinusoid is fitted to every displacement time series, as the solution of an optimisation problem where the parameters to be found are its amplitude, frequency, phase and offset, as illustrated in Fig. 3 for an example of duration comparable to that of a typical measurement. The optimisation problem is formulated as a nonlinear least-squares problem with bounds on the amplitude, frequency, phase and offset variables. The initial guesses for the frequency and phase are the result of a discrete Fourier transform. The initial guess for the bias is computed as the arithmetic mean of the values, and the initial guess for the amplitude as their variance multiplied by $\sqrt{2}$. The solution of the optimisation problem is carried out in a python-based environment, using the implementation in Ref. [20]. As a consequence, computing transfer functions reduces to a complex division of the phasors expressing the motion of the sample with the phasors representing the motion of the foundation. This also allows to reject data points that are deemed of low quality, i.e. data points whose estimated frequency deviates significantly from the excitation frequency.

3. Model of the material

3.1. Constitutive equation

The constitutive laws for fluid-saturated porous materials may be derived as a special case of Biot's equations for anisotropic porous materials including a solid and a fluid phase [8]. The solid and fluid phases are assumed independent and spatially homogeneous at scales of wavelengths much larger than the pore size. For a porous material under vacuum conditions with zero pressure, Hooke's law can be used to provide a causal representation of the stiffness matrix of the materials with a linear superposition of an elastic part, accounting for the frequency-independent fully-relaxed state of the material, and an anelastic part, accounting for frequency-dependent reversible viscoelastic deformation. This has been used in the past in order to estimate various properties of the frame of porous materials without the influence of air [2,4,5,10]. The simplified fractional derivative approach in Ref. [10] is used here. The constitutive equation of the anisotropic materials in the frequency domain is thus given by

$$\sigma_i(\omega) = H_{ij}(\omega)\varepsilon_j(\omega), \quad (1)$$

with

$$\sigma = [\sigma_{11} \ \sigma_{22} \ \sigma_{33} \ \sigma_{12} \ \sigma_{13} \ \sigma_{23}]^T, \quad (2)$$

$$\varepsilon = [\varepsilon_{11} \ \varepsilon_{22} \ \varepsilon_{33} \ 2\varepsilon_{12} \ 2\varepsilon_{13} \ 2\varepsilon_{23}]^T, \quad (3)$$

where σ is a vector containing the stresses associated to the strain state expressed in the vector ε for a material described by a frequency-dependent stiffness matrix H , $\omega = 2\pi f$ being the circular frequency. The strain and stress tensors are symmetric, as such they are represented in Eqs. (2) and (3) as six-element vectors, the subscripts 1, 2, 3 identifying respectively directions x, y, z [24].

The components of the frequency-dependent stiffness matrix are given by

$$H_{ij}(\omega) = C_{ij} + \frac{B_{ij} (i\omega/\beta)^\alpha}{1 + (i\omega/\beta)^\alpha}, \quad (4)$$

where C_{ij} denotes the components of the fully-relaxed stiffness matrix, α is the fractional derivative order, β is the relaxation frequency in $\text{rad}\cdot\text{s}^{-1}$. The stiffness matrix provides a model of the deformation of the material as a superposition of its fully relaxed state and a complex frequency-dependent relaxation phenomenon. In general, a given material may present different types of anisotropy in the elastic and anelastic phenomena. However, both phenomena share the same microstructural geometry and therefore it is here assumed that the elastic and anelastic parts of the stiffness matrix are collinear,

$$B_{ij} = b C_{ij}, \quad (5)$$

where b is a real scalar constant. Then the final form of the stiffness matrix is [10]

$$H_{ij}(\omega) = C_{ij} \left(1 + \frac{b(i\omega/\beta)^\alpha}{1 + (i\omega/\beta)^\alpha} \right), \quad (6)$$

$$H_{ij}(\omega) = H_{ij}^{(R)} + iH_{ij}^{(I)}, \quad (7)$$

where $H_{ij}^{(R)}$ and $H_{ij}^{(I)}$ are respectively the real and imaginary parts of the complex Hooke's matrix $\mathbf{H}(\omega)$.

The Hooke's matrix must be positive definite according to the second law of thermodynamics, thus the real part of the Hooke's matrix must satisfy the following constraints [18],

$$H_{ii}^{(R)} > 0, \quad i = 1, \dots, 6, \quad (8)$$

$$g_j(\mathbf{H}^{(R)}) - 1 < 0, \quad j = 1, \dots, 4, \quad (9)$$

$$\det(\mathbf{H}^{(R)}) > 0, \quad (10)$$

$$b > 0, \quad \alpha > 0, \quad \beta > 0. \quad (11)$$

with

$$g_1 = \frac{(H_{23}^{(R)})^2}{H_{22}^{(R)}H_{33}^{(R)}}, \quad g_2 = \frac{(H_{13}^{(R)})^2}{H_{11}^{(R)}H_{33}^{(R)}}, \quad g_3 = \frac{(H_{12}^{(R)})^2}{H_{11}^{(R)}H_{22}^{(R)}}, \quad (12)$$

$$g_4 = g_1 + g_2 + g_3 - 2 \frac{H_{12}^{(R)}H_{23}^{(R)}H_{31}^{(R)}}{H_{11}^{(R)}H_{22}^{(R)}H_{33}^{(R)}}. \quad (13)$$

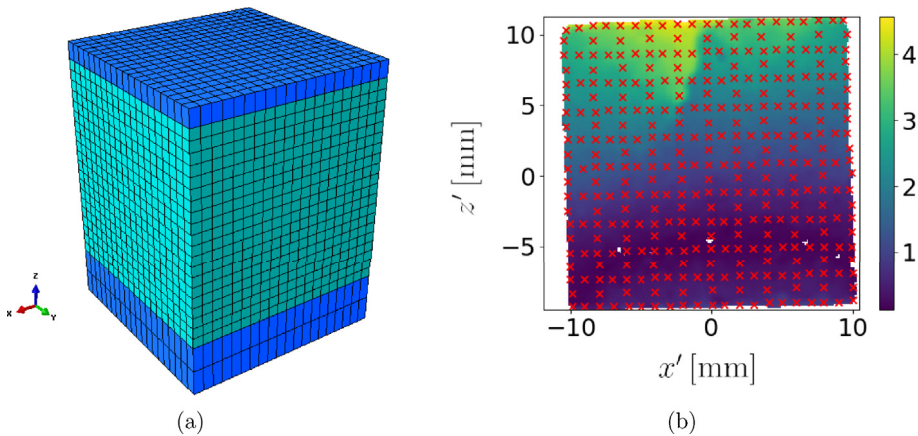


Fig. 4. (a) Finite element mesh of the system and (b) magnitude of the PCA-corrected displacement in the z direction, expressed in the coordinate system (x', y', z') relative to the initial view of the calibration plate and normalised with respect to the average displacement of the foundation in the same direction. The position of the nodal points of the numerical model are overlaid to the rectified face of the sample. The coordinate values on the axes are in millimetres, while the normalised amplitude is dimensionless.

3.2. Finite element model

Fig. 4a shows the finite element mesh used for the simulation model. The foundation and the seismic mass are considered rigid and therefore they are modelled by two and one element layers, respectively. The material sample is modelled using $20 \times 20 \times 20$ quadratic hexahedral solid elements and continuity is assumed at the interface with the foundation and with the seismic mass. Convergence has been verified through a successive evaluation of four different mesh refinements; 10, 15, 20, 30 elements along each side of the cubic sample; for the highest frequency of interest here, i.e. 360 Hz.

A set of displacements on the four observable surfaces, denoted x_- , x_+ , y_- , and y_+ , are extracted from the experimental setup and used as the target transfer functions. These transfer functions are simulated at the same positions in the numerical model in order to build the objective function for the inverse problem, as detailed in the next section.

4. Design exploration

The anisotropic model has 21 material properties and 3 anelastic parameters to be inversely estimated, assuming material symmetries in Eq. (4), which are gathered in the form

$$\mathbf{x} = [C_{11} \ C_{12} \ C_{22} \ C_{13} \ C_{23} \ C_{33} \ C_{14} \ C_{24} \ C_{34} \ C_{44} \ C_{15} \ C_{25} \ C_{35} \ C_{45} \ C_{55} \ C_{16} \ C_{26} \ C_{36} \ C_{46} \ C_{56} \ C_{66} \ b \ \alpha \ \beta]. \quad (14)$$

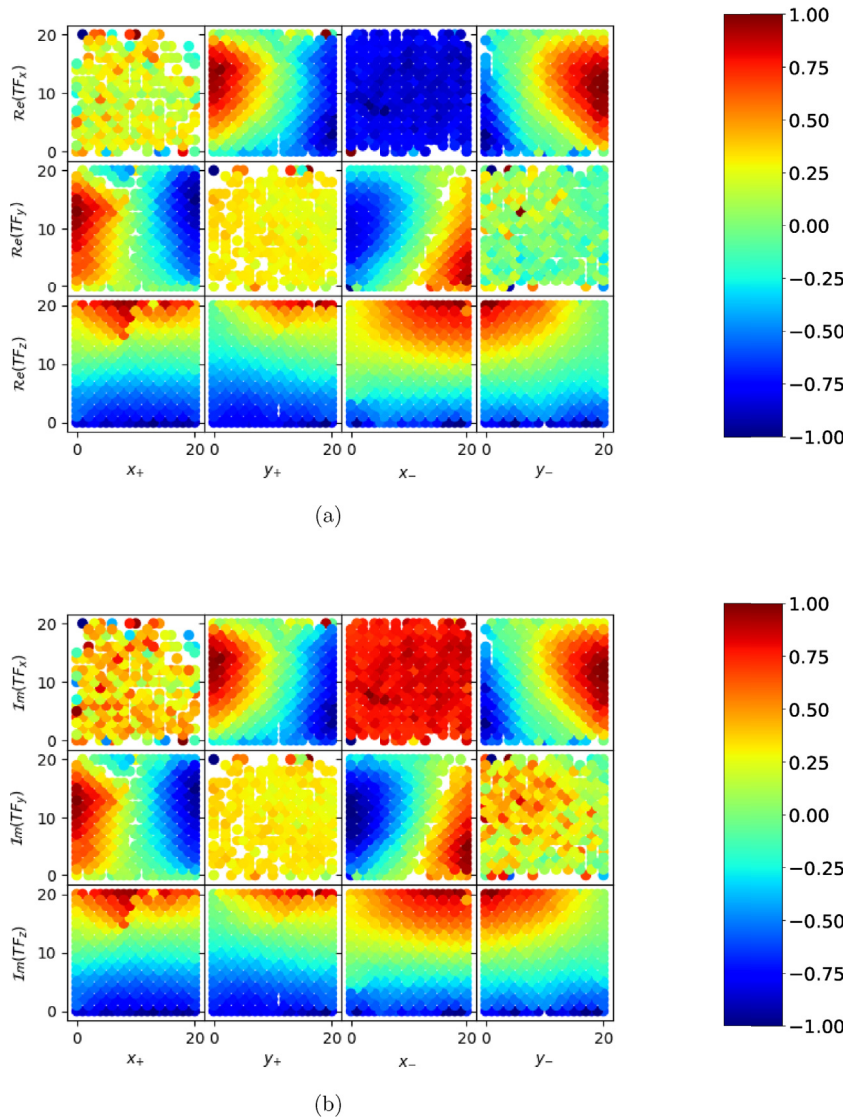


Fig. 5. Experimentally measured transfer functions at 205 Hz. Levels are normalised to the maximum displacement value within each individual face plot. (a) real and (b) imaginary part.

Hence, the model has a 24-dimensional parameter space \mathbf{x} . The model thus allows to simulate a set of transfer functions

$$TF_m(\mathbf{x}, \omega_n, \mathbf{r}_p) = \frac{u_m(\mathbf{x}, \omega_n, \mathbf{r}_p)}{u_z(\omega_n, \mathbf{r}_0)}, \tag{15}$$

where $n \in [1, N]$ denote a set of selected frequencies, $p \in [1, P]$ are the points on the surface of the material where the transfer functions are evaluated and $m \in [x, y, z]$ denote the direction of the displacement field at the selected points. A unit input displacement is prescribed at the foundation in the numerical model.

Accordingly, the experimentally acquired transfer functions are denoted

$$TF_m^{(exp)}(\omega_n, \mathbf{r}_p) = \frac{u_m^{(exp)}(\omega_n, \mathbf{r}_p)}{u_z^{(exp)}(\omega_n, \mathbf{r}_0)}. \tag{16}$$

5. Results

To show the increased resolving power of the presented observation method, selected experimentally measured transfer functions (Eq. (16)) are shown in Figs. 5–7 for the locations at the nodal points of the numerical model. The choice of the observation frequencies is arbitrary, and does not necessarily correspond to natural frequencies of the sample nor the setup.

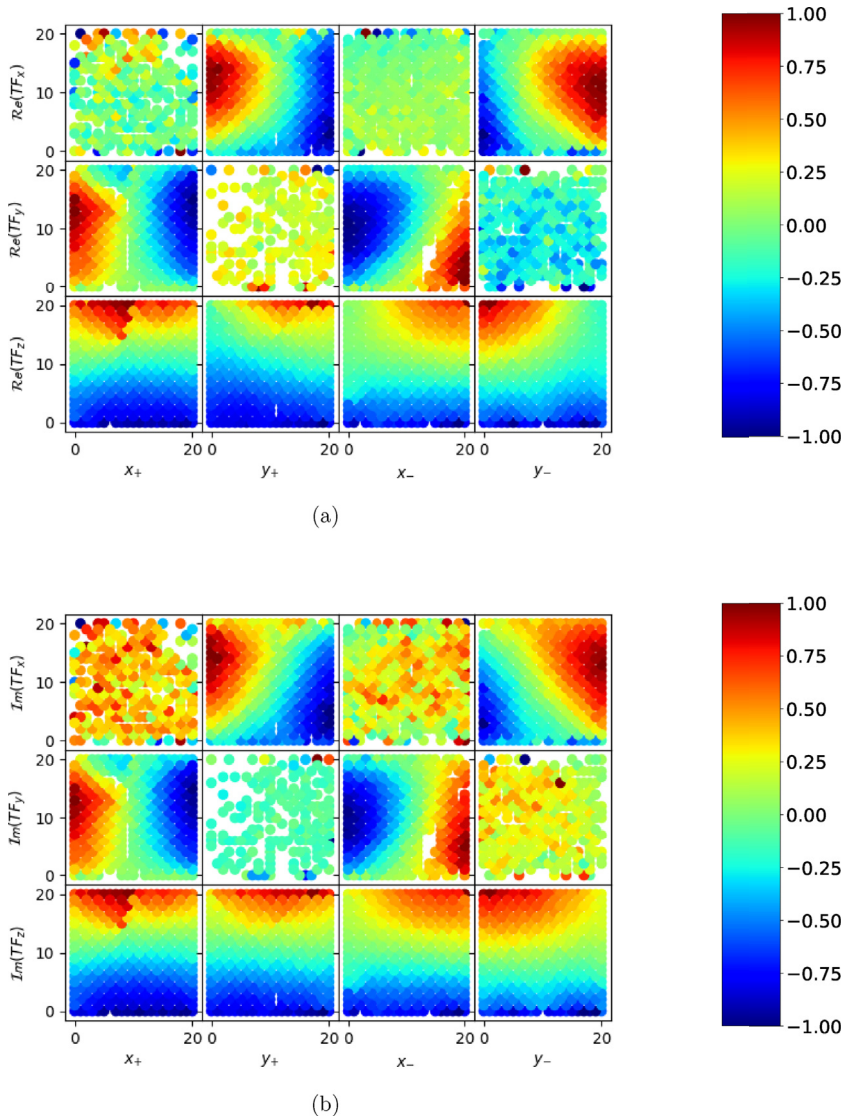


Fig. 6. Transfer functions at 225 Hz, otherwise same caption as in Fig. 5.

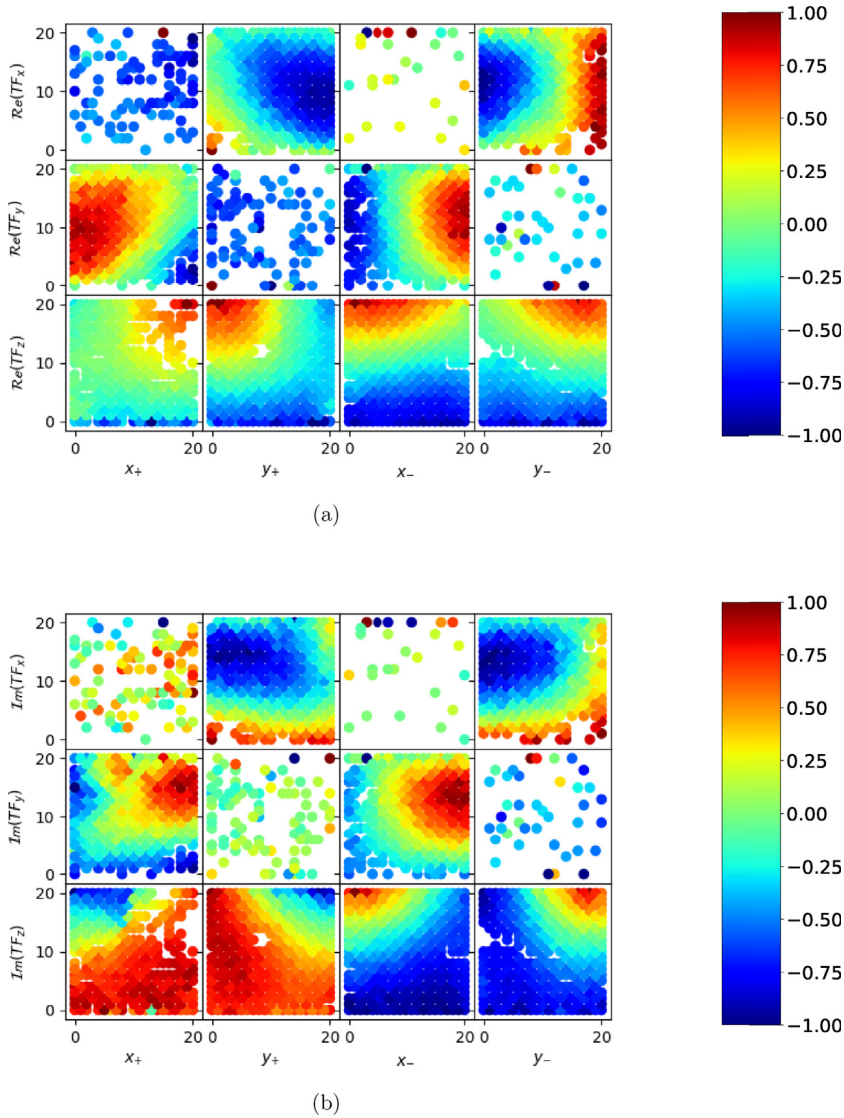


Fig. 7. Transfer functions at 345 Hz, otherwise same caption as in Fig. 5.

Note that the ranges are chosen such that the highest value in any point on a subplot, i.e. a face of the cube, is normalised to unity. This choice was made in order to appreciate local spatial variations of each of the fields as such, at the expense of relative information across the different displacement components. Absent points indicate locations where no reliable estimate could be obtained based on the proposed method for processing the DIC data, see Sect. 2.2.

The in-plane deformations are well identified for the two lower frequencies, Figs. 5 and 6, while some points are missing in the 345 Hz results, Fig. 7. This is most probably due to the excitation level being too low at this latter frequency, due to the amplitude of the signal driving the power amplifier (thus the shaker) being constant for all frequencies. The out-of-plane displacements; see e.g. Fig. 5a, first row, first and third columns; or second row, second and fourth columns; etc.; are rather uniform over the faces of the cubic sample, even though some points artificially appear to distort the fields in the presentation format chosen here. One of the open questions for the present work, is whether temporal information contained in a spectrum of a few points may be exchanged for spatial information at a few frequencies with comparable or better suitability for a parameter estimation procedure. For all three frequencies shown here, the data obtained confirm that the spatial variation is well captured, indeed showing the expected deformation patterns of a material having elastic properties which are directionally dependent. Perhaps the most prominent indication of this, in the present data, may be the in-plane deformations in Fig. 7a, first row, second and fourth columns; or Fig. 7b third row.

The experimentally measured transfer functions are compared with the outcome from a previously obtained model [10], where the linear elastic Hooke's matrix for the melamine foam investigated here was shown to be represented by a general

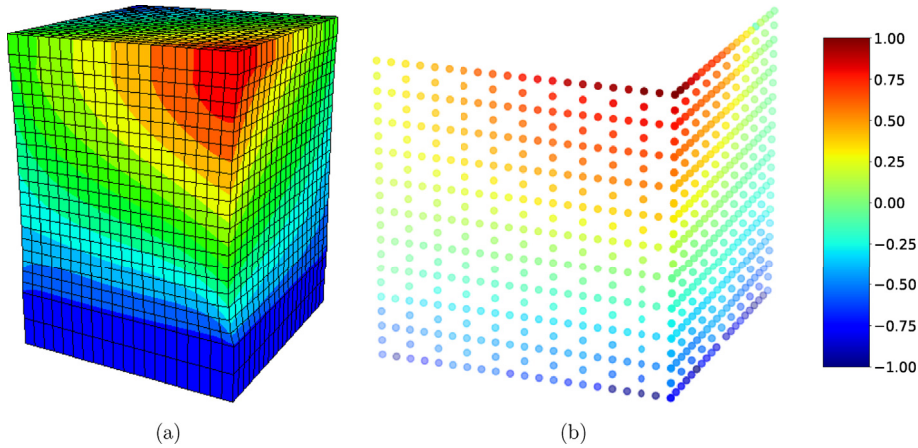


Fig. 8. Real part of the displacement in z -direction for faces x_- and y_+ at 205 Hz, (a) from the finite element model (b) from the experimental data.

orthotropic material, as

$$\mathbf{C} = [C_{ij}] = \begin{bmatrix} 4.2 & 1.2 & 3.4 & 0.08 & -0.55 & 0.06 \\ & 2.2 & 0.06 & 0.02 & -0.01 & -0.28 \\ & & 7.6 & 0.11 & -0.94 & 0.8 \\ & & & 1.2 & 0.01 & 0.04 \\ \text{(sym)} & & & & 1.1 & -0.04 \\ & & & & & 1.1 \end{bmatrix} 10^6 \text{ Pa}, \quad (17)$$

and the fractional derivative model, Eq. (4), used to represent the relaxation was found to be

$$b = 0.296, \beta = 813 \text{ krad/s}, \alpha = 0.333. \quad (18)$$

Using these input data, as a means of assessing the correspondence between the previous experimental campaign and the currently extracted experimental data, finite element simulations were performed on the same geometry and excitation as in the test setup. An example of the results obtained is shown in Fig. 8, where the real parts of the displacement fields from the finite element and the measurements are shown.

From a qualitative point of view the agreement is quite encouraging. Still, the lower sensitivity to shear of the laser-based measurements becomes apparent when observing the transfer functions as a function of z -coordinate, Fig. 9. Effectively, the previously employed measurement technique only allowed access to the data points at $z = 0$ mm and $z = 20$ mm. The currently available amount of experimental data is directly comparable with numerical simulations at significantly more locations in space as compared to a set of single-point observations. As pointed-out in the introduction, the motivation behind such abundance of measurement data is a correspondingly over-determined model inversion procedure. Nevertheless, the purpose of the current paper being to present the experimental methodology, the expected improvements in terms of estimated parameters and robustness of the inverse estimation procedure will be evaluated in future work. Similarly, the increased amount of data may allow for a relaxation of the elastic-anelastic collinearity hypothesis [9,10], thus potentially yielding more truthful material characterisations in a less constrained manner.

6. Conclusion

The present paper proposes an experimental method for obtaining full-field observations of the dynamic behaviour of anisotropic open-cell porous materials by means of digital image correlation. In practice, an automated test rig has been developed and tested on a sample of melamine foam. The experimental procedure allows for the sequential measurement of the displacement of the four visible faces of the material sample. The displacements are estimated as the best fit of a sinusoidal function on the digital image correlation time signals, which allows to deal with short acquisition times and to reject measurement points where the signal does not have a causal relation with the excitation. The measurement system is able to resolve displacements in three dimensions both for the sample and the foundation, thus allowing to extract transfer functions from within the frames of the camera acquisitions. Furthermore, a principal component analysis is applied to the ensemble of displacement points obtained for the foundation in order to extract the motion of the sample in the coordinate system relative to the foundation.

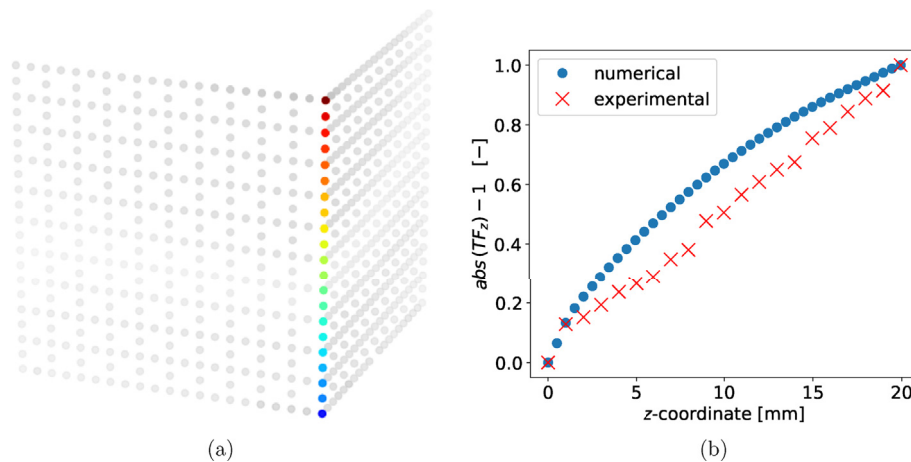


Fig. 9. Comparison of the normalised magnitude of the transfer functions in the z -direction at 205 Hz as obtained from the finite element model and from the experimental data, as a function of z -coordinate (b), for the set of points highlighted in (a).

A numerical model replicating the setup has been built which allows to reproduce the experimental behaviour of the material, based on an augmented Hooke's law formulation including the anelastic properties of the anisotropic open-cell foam in vacuum. A fully anisotropic model has been used, thus allowing for exploring the model without symmetry constraints.

A qualitative agreement of the experimental and numerical transfer functions has been observed, with an emphasis of the importance of an increased resolving power in view of an augmentation of the inverse estimation procedure proposed in Ref. [10]. In particular, the present method is shown to capture spatial variations in the dynamic deformation field not previously accessible with measurements relying on a set of single-point observations. It is expected that the abundance of data will reduce the complexity of a subsequent inverse estimation procedure in terms of limiting the appearance of local minima.

Acknowledgments

Part of the funding for this work is received under the Swedish Research Council, Grant No. 2015-04258. The authors also acknowledge the funding provided by the Knut and Alice Wallenberg Foundation, in the form of the MUSCLE project awarded to the Odqvist Laboratory in which the equipment used in the current research has been funded.

References

- [1] J. Allard, N. Atalla, *Propagation of Sound in Porous Media: Modelling Sound Absorbing Materials 2e*, Wiley, 2009.
- [2] T. Pritz, Frequency dependence of frame dynamic characteristics of mineral and glass wool materials, *J. Sound Vib.* 106 (1) (1986) 161–169.
- [3] T. Pritz, Dynamic Young's modulus and loss factor of plastic foams for impact sound isolation, *J. Sound Vib.* 178 (3) (1994) 315–322.
- [4] A. Sfaoui, On the viscoelasticity of the polyurethane foam, *J. Acoust. Soc. Am.* 97 (2) (1995) 1046–1052.
- [5] H. Rice, P. Gransson, A dynamical model of light fibrous materials, *Int. J. Mech. Sci.* 41 (45) (1999) 561–579.
- [6] M. Biot, Mechanics of deformation and acoustic propagation in porous media, *J. Appl. Phys.* 33 (4) (1962) 1482–1498.
- [7] M. Biot, Generalized theory of acoustic propagation in porous dissipative media, *J. Acoust. Soc. Am.* 34 (9) (1962) 1254–1264.
- [8] M.A. Biot, Theory of propagation of elastic waves in a fluid-saturated porous solid. i. low-frequency range, *J. Acoust. Soc. Am.* 28 (2) (1956) 168–178.
- [9] J. Cuenca, P. Gransson, Inverse estimation of the elastic and anelastic properties of the porous frame of anisotropic open-cell foams, *J. Acoust. Soc. Am.* 132 (2) (2012) 621–629.
- [10] J. Cuenca, C. Van der Kelen, P. Gransson, A general methodology for inverse estimation of the elastic and anelastic properties of anisotropic open-cell porous materials with application to a melamine foam, *J. Appl. Phys.* 115 (8) (2014) 084904.
- [11] P. Bonfiglio, F. Pompili, K.V. Horoshenkov, M.I.B.A. Rahim, L. Jaouen, J. Rodenas, F.-X. Bcot, E. Gourdon, D. Jaeger, V. Kursch, M. Tarello, N.B. Roozen, C. Glorieux, F. Ferriani, P. Leroy, F.B. Vangosa, N. Dauchez, F. Foucart, L. Lei, K. Carillo, O. Dautres, F. Sgard, R. Panneton, K. Verdiere, C. Bertolini, R. Br, J.-P. Groby, A. Geslain, N. Poulain, L. Rouleau, A. Guinault, H. Ahmadi, C. Forge, How reproducible are methods to measure the dynamic viscoelastic properties of poroelastic media? *J. Sound Vib.* 428 (2018) 26–43.
- [12] L. Jaouen, A. Renault, M. Deverge, Elastic and damping characterizations of acoustical porous materials: available experimental methods and applications to a melamine foam, *Appl. Acoust.* 69 (12) (2008) 1129–1140.
- [13] E. Lundberg, *Micro-structure Modelling of Acoustics of Open Porous Material*, 2016.
- [14] N. Kino, T. Ueno, Comparisons between characteristic lengths and fibre equivalent diameters in glass fibre and melamine foam materials of similar flow resistivity, *Appl. Acoust.* 69 (4) (2008) 325–331.
- [15] P. Martin, S. Rothberg, Laser vibrometry and the secret life of speckle patterns, in: *Proceedings of SPIE - the International Society for Optical Engineering*, vol. 7098, 2008, p. 709812.
- [16] L. Manzari, P. Gransson, J. Cuenca, I. Lopez Arteaga, A fully automated high-speed optical rig for in vacuo, full field, non-contact vibration measurements for viscoelastic, anisotropic materials, in: *NOVEM 2018 Proceedings Noise and Vibration Emerging Methods the 6th Conference*, 2018, pp. 91–102.
- [17] L. Manzari, P. Gransson, J. Cuenca, I.L. Arteaga, Toward fully anisotropic viscoelastic material models using an automated high-speed optical rig, *J. Phys. Conf.* 1149 (2018) 012003.
- [18] R.M. Jones, *Mechanics of Composite Materials*, Taylor & Francis, Philadelphia, 1999.
- [19] C. Van der Kelen, J. Cuenca, P. Gransson, A method for the inverse estimation of the static elastic compressional moduli of anisotropic poroelastic foams with application to a melamine foam, *Polym. Test.* 43 (2015) 123–130.

- [20] M.A. Branch, T.F. Coleman, Y. Li, A subspace, interior, and conjugate gradient method for large-scale bound-constrained minimization problems, *SIAM J. Sci. Comput.* 21 (1) (1999) 1–23.
- [21] LaVision GmbH, Product-Manual for DaVis 8.3, Imaging Tools, 2015.
- [22] LaVision GmbH, Product-Manual for DaVis 8.4, StrainMaster, 2017.
- [23] S.M. Soloff, R.J. Adrian, Z.-C. Liu, Distortion compensation for generalized stereoscopic particle image velocimetry, *Meas. Sci. Technol.* 8 (12) (1997).
- [24] O.A. Bauchau, J.I. Craig, *Structural Analysis with Applications to Aerospace Structures*, Springer, 2009.